# MOCCA

a Multi-sourced Ocean Carbonate Chemistry Analysis

Friedrich Burger

June 10, 2024

## Contents



## 1 Introduction

Deep learning has been heavily used in climate science in recent years (Reichstein et al., 2019), with applications ranging from forecasting, statistical down-scaling, pattern identification, process parameterization, emulation of physical models, to data interpolation. The success of deep learning in such data-driven applications is based on the versatility of neural networks Goodfellow et al. (2016). In theory, these can be used to learn any functional relationship between predictors and variables of interest, as reflected by the universal approximation theorem Hornik et al. (1989).

A particularly important application of deep learning is the interpolation of sparse ship-based measurements of the fugacity of carbon dioxide ($fCO_2$) in the surface ocean. A globally consistent and complete field of $fCO_2$ is necessary to estimate the air-sea $CO_2$ flux and thus necessary to estimate the fraction of anthropogenic carbon emissions that is taken up by the ocean. The global carbon budget (Friedlingstein et al., 2023), an annual assessment of global carbon emissions and sinks, currently estimates the oceanic sink from seven observation-based products. While based on very similar underlying fCO2 data

and similar mostly satellite-based predictors, these seven products follow different approaches for interpolating the sparse $fCO_2$ data.

Four of these products are based on feed-forward neural networks: The CMEMS-LSCE-FFNNv2 (Chau et al., 2022) utilizes a 100-member neural network ensemble, bootstrapping from the months before and after a $fCO_2$ measurements and leaving the months with $fCO_2$ measurements for independent evaluation. The MPI-SOMFFN (Landschützer et al., 2016) builds on a two step procedure, where first different clusters of similar ocean conditions are determined using a self-organizing map approach and then neural networks are trained to predict $fCO_2$ in each cluster separately. Similarly, OS-ETHZ-GRaCER (Gregor and Gruber, 2021) provides an ensemble of varying cluster assignments with neural-network-based $fCO_2$ regression in each cluster. NIES-ML3 (Zeng et al., 2022) is based on three model estimates, from a random forest, a gradient boost machine, and a feed-forward neural network. The remaining three observation-based products build on multiple linear regressions for $A_T$ and $C_T$ (fundamental variables to calculate $fCO_2$ and other carbonate system variables; JMA-MLR; Iida et al., 2021), extreme gradient boosting to predict the missfit between global ocean biogeochemical models and $fCO_2$ measurements (LDEO-HPD; Gloege et al., 2022), and a autoregressive multiple linear regression approach (Jena-MLS; Rödenbeck et al., 2022).

The largest uncertainty in these spatially and temporally interpolated $fCO_2$ fields roots in the sparsity and uneven distribution of the underlying $fCO_2$ measurements that are collected in the Surface Ocean $CO_2$ Atlas (Bakker et al., 2016). In particular, measurements are sparse in high-latitude regions and particularly in the Southern Ocean. One approach to soften this issue is applying neural-network based regression seprately in clusters with similar ocean-biogeochemical conditions (Landschützer et al., 2016; Gregor and Gruber, 2021), grouping data-sparse regions with others with similar conditions. MOCCA, instead, attempts to tackle these limitations by not only using $fCO_2$ measurements for training, but also pH measurements from biogeochemical Argo floats (Johnson et al., 2017), which provide critical additional data in the Southern Ocean, and other biogeochemical data as provided by the Global Ocean Data Analysis Project (GLODAPv2; Olsen et al., 2016). Furthermore, the neural network in MOCCA is pretrained on CMIP6 Earth system models to foster inference of surface $fCO_2$ in sparsely sampled ocean regions with the prior knowledge about functional relationships from Earth system models. The use of multiple sources of data is enabled by a flexible model structure that allows to train on multiple target variables. Similarly to Iida et al. (2021), this flexible approach also provides coherent estimates for all variables of the oceanic carbonate system.

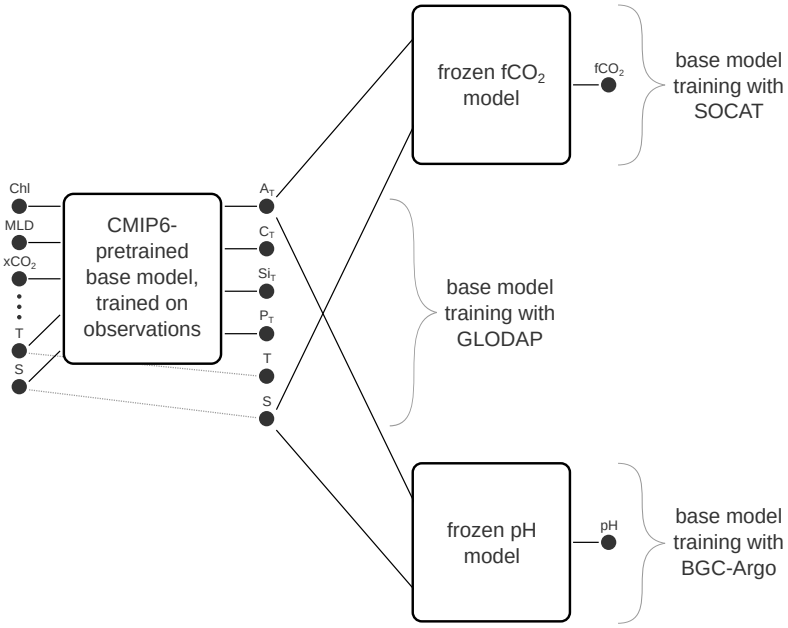


Figure 1: Scheme displaying the overall model architecture of MOCCA.

# 2 Model architecture

## 2.1 Overview

MOCCA is based on a three-step procedure (Figure 2). In a first step, surrogate neural network models are trained to fit the functional relationship between a set of variables needed to solve the oceanic carbonate system (*carbonate chemistry drivers*) and two specific carbonate chemistry variables, pH and fugacity of $CO_2$ (Section 2.2). The functional relationship is learned from the numerical carbonate chemistry package *mocsy 2.0* (Orr and Epitalon, 2015). This step is performed first to identify appropriate hyper parameters and training procedure in a situation where near-perfect learning is possible.

In a second step, a neural network is trained on model output from CMIP6 Earth system models to learn the statistical relationships between a set of predictors and the carbonate chemistry drivers. This model will serve as a prior estimate to improve inference for $fCO_2$ and pH in undersampled regions where only few $fCO_2$ and pH measurements are available.

In a third step, the CMIP6-pretrained model from the previous step is trained with observational data for $fCO_2$ from the Surface Ocean $CO_2$ Atlas (SOCAT), carbonate chemistry drivers from GLODAP, and pH from BGC-Argo floats. To do so, the loss is either directly calculated from the output of the base model (GLODAP), or the $fCO_2$ or pH models are appended to the base model (for SOCAT and BGC-Argo respectively).In the latter case, the layers of the $fCO_2$ or pH models are frozen to prevent further parameter updates.

## 2.2 Surrogate models for mocsy fCO2 and pH

In a first step, surrogate multi-layer perceptron models were trained to replace numerical solution of the oceanic carbonate system. To do so, samples for total alkalinity ($A_T$), dissolved inorganic carbon ($C_T$), temperature (T), salinity (S), total silicate ($Si_T$), and total phosphate ($P_T$) were randomly generated from uniform distributions (Table 1).
The training data size was set to 5 000 000 samples and the validation data size was set to 1 000 000 samples. Mocsy 2.0 (Orr et al., 2015a) was then used to calculate $fCO_2$ and pH for these samples. After normalizing per feature with the means and standard deviations given in Table 1, multilayer perceptron models with three identical hidden layers were trained with mocsy $fCO_2$ and pH as labels.
For $fCO_2$, model complexity was iteratively increased until a desired maximum deviation of less than 1 $\mu$atm was reached (the measurement uncertainty for $pCO_2$ as reported by Orr et al, 2015b)[1]. During training, learning rate was decreased from $10^{-3}$ to $10^{-5}$ following an exponential learning rate schedule over 10 000 epochs. The decay in learning rate was chosen to shift from an initial identification of an optimal region in the parameter space to finding an

[1]For reference, $fCO_2$ across the generated samples varies between 0.001 $\mu$atm and 5108 $\mu$atm.

| | minimum | maximum |
|---|---|---|
| $A_T$ | $1000\,\mu mol\,kg^{-1}$ | $3000\,\mu mol\,kg^{-1}$ |
| $C_T$ | $1000\,\mu mol\,kg^{-1}$ | $A_T$ |
| T | -2 °C | 35 °C |
| S | 10 PSU | 50 PSU |
| $Si_T$ | $0\,\mu mol\,kg^{-1}$ | $134\,\mu mol\,kg^{-1}$ |
| $P_T$ | $0\,\mu mol\,kg^{-1}$ | $4\,\mu mol\,kg^{-1}$ |

Table 1: Minima and maxima of the uniform distributions used to generate samples for the $fCO_2$ and pH surrogate models. The range for $A_T$ was chosen such that it easily encompasses open ocean variations in $A_T$. That for $C_T$ is limited to values lower $A_T$ since larger $C_T$ do not occur in the ocean. The ranges for T and S are chosen according to Lueker et al., 2000, whose parameterizations for $K_1$ and $K_2$ are used in mocsy. Finally, the maximum values for $Si_T$ and $P_T$ were chosen to be the global maxima found in the monthly climatologies for $Si_T$ and $P_T$ from World Ocean Atlas 2023. These uniform distributions have means $(max + min)/2$ and standard deviations $(max - min)/\sqrt{12}$, expcept for $C_T$ where mean and standard deviation are given by $min + (max - min)/4$ and $(max - min) \cdot \sqrt{7/144}$, respectively. These means and standard deviations are used for feature normalization.

optimal set of parameters for which the mean squared error over the training and validation sets converges to a similar and low value.
Hidden layer size was increased from an initial 64 hidden layer units (8833 trainable parameters), 80 units (13601 parameters), 96 units (19393 parameters), 128 units (34049 parameters), to 160 units (52801 parameters). The largest model[2] hit a maximum deviation of $1.08\,\mu atm$ over the validation set (Figure 2). The same model architecture was then also used to train the pH model, resulting in a maximum deviation over the validation set of 0.0044.
With root mean squared errors (RMSE) of $0.026\,\mu atm$ ($fCO_2$ model) and 0.00008 (pH model), these surrogate models provide a precision that is comparable to numerical carbonate chemistry packages: Orr et al., 2015b report a desired numerical uncertainty of $0.1\,\mu atm$ and 0.0003, respectively.
The accurracy of the $fCO_2$ and pH neural network models is similar for the six million random samples for $A_T$, $C_T$, T, S, $Si_T$, and $P_T$ from the CMIP6 models (section 2.3). Specifically, RMSE is $0.029\,\mu atm$ and 0.00006, respectively, and the maximum deviations are $0.24\,\mu atm$ and 0.0006, respectively.

[2]To give some context about the model complexity: The number of paramters of this model is comparable to that of a Taylor expansion of a function with six arguments to 15th order. Assuming an efficient use of the MLP parameters, a good fit to the numerical solution from mocsy is thus expected.

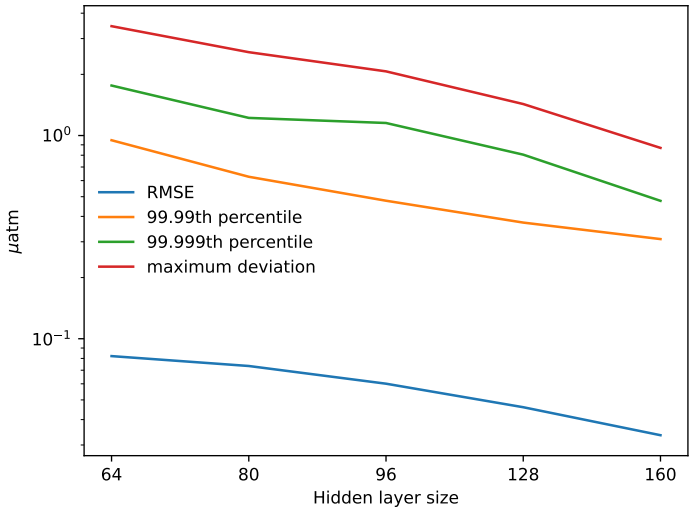


Figure 2: The evolution of root mean squared error (RMSE), the 99.99th and 99.999th percentiles of deviation and the maximum deviation between the surrogate model and mocsy $fCO_2$ over the validation data set with 1000 000 randomly generated samples.

## 2.3 CMIP6-pretrained base model

As a first step, we pre-train a neural network on the statistical relationships between predictor variables and sea surface $A_T$, $C_T$, $Si_T$, and $P_T$. The predictor variables chosen here are sea surface temperature (SST), sea surface salinity (SSS), mixed layer depth (MLD), sea surface height (SSH), chlorophyll-a concentration (chl), sea ice concentration (ice), 10 m easterly wind (u), 10 m northerly wind (v), dry volume molar ratio of $CO_2$ in the atmosphere ($CO_2$), sinus and cosinus of the month of year ($\sin(m/12 \cdot 2\pi)$ and $cos(m/12 \cdot 2\pi)$), as well as latitude and longitude encoded using spherical coordinates following Gade (2010). The representations for month of year and location are used to avoid discontinuities in the months between December and January and in longitude at the dateline (±180 °E).

The neural network is trained on 6 million samples (5 million for training and 1 million for validation) that were evenly drawn from three CMIP6 Earth system models: the UKESM1-0-LL, the MPI-ESM1-2-LR, and the CMCC-ESM2. Despite a high-resolution version of the MPI model, these were the only ones to provide all predictors on monthly-mean resolution. Data from multiple Earth system models were used to ensure that the model learns general relationships that are not specific to a certain Earth system model with respective biases. The model data is taken from the period 1993-2022 (*historical* simulation until 2014, followed by *SSP2-4.5*). The predictors MLD and chl were log-transformed prior to training to foster learning. The log transformation was applied only where the resulting distribution was more Gaussian (where the test statistic of a Kolmogorov-Smirnov test, i.e. the maximum difference between the empirical distribution function of the data and the distribution function of a standard normal distribution, was smaller after transformation). Finally the predictors for the CMIP6 pre-trained base model are nromalized to zero mean and unit variance and the 4 labels are normalized as specified in Table 1 (to match the normalization used for the $fCO_2$ and pH surrogate models).

For the training, the same architecture that was already used to train the surrogate models (despite not applying a final ELU non-linearity on the output layer, such that the last hidden layer is linearly projected) is used, again with 10 000 epochs and a batch size of 1000. Root mean squared errors of 6.1 $\mu$mol kg$^{-1}$ ($A_T$), 6.3 $\mu$mol kg$^{-1}$ ($C_T$), 0.8 $\mu$mol kg$^{-1}$ ($Si_T$), and 0.03 $\mu$mol kg$^{-1}$ ($P_T$) are obtained (on the validation set and after backtransforming to unnormalized labels). As such, RMSEs are more than a magnitude lower than the standard deviations of $A_T$, $C_T$, $Si_T$, and $P_T$ in the CMIP6 model data samples, given by 111.7, 99.1, 26.3, and 0.5 $\mu$mol kg$^{-1}$, respectively[3]. Likely due to the large size of the training data set relative to the model complexity, overfitting appears not to be a problem. The validation loss continuously decreases, ending up 11 % larger than the training loss[4].

[3]RMSE equals the standard deviation for a model that always predicts the mean of a variable. Hence, a lower RMSE implies skill in predicting spatial and temporal variations in the variable.

[4]Technically speaking, the training data loss is calculated for all batches in an epoch

| Predictor | Data product |
|---|---|
| Sea surface temperature | ESA SST CCI and C3S[1] |
| Sea ice fraction | ESA SST CCI and C3S[1] |
| Sea surface salinity | CMEMS ARMOR3D L4[2] |
| Mixed layer depth | CMEMS ARMOR3D L4[2] |
| Sea surface height | CMEMS L4 Sea Surface Heights[3] |
| Chlorophyll-a concentration | Copernicus-GlobColour[4] |
| $CO_2$ mole fraction | CAMS CO2 atmospheric inversion[5] |
| Eastward near-surface wind | ECMWF Reanalysis v5 (ERA5)[6] |
| Northward near-surface wind | ECMWF Reanalysis v5 (ERA5)[6] |

Table 2: List of predictors used to predict $A_T$, $C_T$, $Si_T$, and $P_T$ and the data product used for each predictor. [1]`https://doi.org/10.48670/moi-00169`; only available until Oct. 2022, [2]`https://doi.org/10.48670/moi-00052`, [3]`https://doi.org/10.48670/moi-00148`, [4]`https://doi.org/10.48670/moi-00281`; only available from Sept. 1997 on, [5]`https://atmosphere.copernicus.eu`, [6]`https://www.ecmwf.int/en/forecasts/dataset/ecmwf-reanalysis-v5`

A part of this error can be explained by the fact that the neural network mapping is necessarily imperfect since the three models imply different statistical relationships between predictors and labels. Creating 6 million samples only from the UKESM1-0-LL model, the root mean squared errors become significantly smaller, now being $4.0\,\mu\mathrm{mol\,kg^{-1}}$ for $A_T$, $4.2\,\mu\mathrm{mol\,kg^{-1}}$ for $C_T$, $0.5\,\mu\mathrm{mol\,kg^{-1}}$ for $Si_T$, and $0.02\,\mu\mathrm{mol\,kg^{-1}}$ for $P_T$. The remaining errors should be mainly due to insufficient information in the predictor variables to fully explain the variations in the four concentrations. As such, it can be assumed that no observation-based regression based on these predictors will perform significantly better. Adding further predictors may still enhance the skill of a model. However, an experiment with total cloud cover and precipitaion as additional atmospheric predictors resulted only in marginal improvements of errors.

## 2.4 SOCAT-, GLODAP-, and BGC-Argo-based model tuning

The data products used for each predictor are listed in Table 2.

separately and then averaged. It is thus calculated slightly different than the validation loss.

| Label | Data product |
|---|---|
| fCO2 | SOCATv2023[1] |
| $A_T$, $C_T$, $Si_T$, $P_T$ | GLODAPv2 2023[2] |
| pH | BGC-Argo[3] |

Table 3: List of label data used to train the base model. [1]`https://socat.info/index.php/2023/06/20/v2023-release/`, [2]`https://glodap.info/index.php/merged-and-adjusted-data-product-v2-2023/`, [3]`https://www.seanoe.org/data/00311/42182/`

# 3 Model performance

# 4 Discussion and conclusions

# References


D. C. E. Bakker, B. Pfeil, C. S. Landa, N. Metzl, K. M. O'Brien, A. Olsen, K. Smith, C. Cosca, S. Harasawa, S. D. Jones, S. Nakaoka, Y. Nojiri, U. Schuster, T. Steinhoff, C. Sweeney, T. Takahashi, B. Tilbrook, C. Wada, R. Wanninkhof, S. R. Alin, C. F. Balestrini, L. Barbero, N. R. Bates, A. A. Bianchi, F. Bonou, J. Boutin, Y. Bozec, E. F. Burger, W.-J. Cai, R. D. Castle, L. Chen, M. Chierici, K. Currie, W. Evans, C. Featherstone, R. A. Feely, A. Fransson, C. Goyet, N. Greenwood, L. Gregor, S. Hankin, N. J. Hardman-Mountford, J. Harlay, J. Hauck, M. Hoppema, M. P. Humphreys, C. W. Hunt, B. Huss, J. S. P. Ibánhez, T. Johannessen, R. Keeling, V. Kitidis, A. Körtzinger, A. Kozyr, E. Krasakopoulou, A. Kuwata, P. Landschützer, S. K. Lauvset, N. Lefèvre, C. Lo Monaco, A. Manke, J. T. Mathis, L. Merlivat, F. J. Millero, P. M. S. Monteiro, D. R. Munro, A. Murata, T. Newberger, A. M. Omar, T. Ono, K. Paterson, D. Pearce, D. Pierrot, L. L. Robbins, S. Saito, J. Salisbury, R. Schlitzer, B. Schneider, R. Schweitzer, R. Sieger, I. Skjelvan, K. F. Sullivan, S. C. Sutherland, A. J. Sutton, K. Tadokoro, M. Telszewski, M. Tuma, S. M. A. C. van Heuven, D. Vandemark, B. Ward, A. J. Watson, and S. Xu. A multi-decade record of high-quality $fco_2$ data in version 3 of the surface ocean $co_2$ atlas (socat). *Earth System Science Data*, 8(2):383–413, 2016. doi: 10.5194/essd-8-383-2016. URL `https://essd.copernicus.org/articles/8/383/2016/`.

T. T. T. Chau, M. Gehlen, and F. Chevallier. A seamless ensemble-based reconstruction of surface ocean $pco_2$ and air–sea $co_2$ fluxes over the global coastal and open oceans. *Biogeosciences*, 19(4):1087–1109, 2022. doi: 10.5194/bg-19-1087-2022. URL `https://bg.copernicus.org/articles/19/1087/2022/`.

P. Friedlingstein, M. O'Sullivan, M. W. Jones, R. M. Andrew, D. C. E. Bakker, J. Hauck, P. Landschützer, C. Le Quéré, I. T. Luijkx, G. P. Peters, W. Peters, J. Pongratz, C. Schwingshackl, S. Sitch, J. G. Canadell, P. Ciais, R. B. Jackson, S. R. Alin, P. Anthoni, L. Barbero, N. R. Bates, M. Becker, N. Bellouin, B. Decharme, L. Bopp, I. B. M. Brasika, P. Cadule, M. A. Chamberlain, N. Chandra, T.-T.-T. Chau, F. Chevallier, L. P. Chini, M. Cronin, X. Dou, K. Enyo, W. Evans, S. Falk, R. A. Feely, L. Feng, D. J. Ford, T. Gasser, J. Ghattas, T. Gkritzalis, G. Grassi, L. Gregor, N. Gruber, O. Gürses, I. Harris, M. Hefner, J. Heinke, R. A. Houghton, G. C. Hurtt, Y. Iida, T. Ilyina, A. R. Jacobson, A. Jain, T. Jarníková, A. Jersild, F. Jiang, Z. Jin, F. Joos, E. Kato, R. F. Keeling, D. Kennedy, K. Klein Goldewijk, J. Knauer, J. I. Korsbakken, A. Körtzinger, X. Lan, N. Lefèvre, H. Li, J. Liu, Z. Liu, L. Ma, G. Marland, N. Mayot, P. C. McGuire, G. A. McKinley, G. Meyer, E. J. Morgan, D. R. Munro, S.-I. Nakaoka, Y. Niwa, K. M. O'Brien, A. Olsen, A. M. Omar, T. Ono, M. Paulsen, D. Pierrot, K. Pocock, B. Poulter, C. M. Powis, G. Rehder, L. Resplandy, E. Robertson, C. Rödenbeck, T. M. Rosan, J. Schwinger, R. Séférian, T. L. Smallman, S. M. Smith, R. Sospedra-Alfonso, Q. Sun, A. J. Sutton, C. Sweeney, S. Takao, P. P. Tans, H. Tian, B. Tilbrook, H. Tsujino, F. Tubiello, G. R. van der Werf, E. van Ooijen, R. Wanninkhof, M. Watanabe, C. Wimart-Rousseau, D. Yang, X. Yang, W. Yuan, X. Yue, S. Zaehle, J. Zeng, and B. Zheng. Global carbon budget 2023. *Earth System Science Data*, 15(12):5301–5369, 2023. doi: 10.5194/essd-15-5301-2023. URL `https://essd.copernicus.org/articles/15/5301/2023/`.

K. Gade. A non-singular horizontal position representation. *THE JOURNAL OF NAVIGATION*, 63:395–417, 2010. ISSN 0021-9991. doi: doi:10.1017/S0373463309990415.

L. Gloege, M. Yan, T. Zheng, and G. A. McKinley. Improved quantification of ocean carbon uptake by using machine learning to merge global models and pco2 data. *Journal of Advances in Modeling Earth Systems*, 14(2):e2021MS002620, 2022. doi: https://doi.org/10.1029/2021MS002620. URL `https://agupubs.onlinelibrary.wiley.com/doi/abs/10.1029/2021MS002620`. e2021MS002620 2021MS002620.

I. J. Goodfellow, Y. Bengio, and A. Courville. *Deep Learning*. MIT Press, Cambridge, MA, USA, 2016. `http://www.deeplearningbook.org`.

L. Gregor and N. Gruber. Oceansoda-ethz: a global gridded data set of the surface ocean carbonate system for seasonal to decadal studies of ocean acidification. *Earth System Science Data*, 13(2):777–808, 2021. doi: 10.5194/essd-13-777-2021. URL `https://essd.copernicus.org/articles/13/777/2021/`.

K. Hornik, M. Stinchcombe, and H. White. Multilayer feedforward networks are universal approximators. *Neural Networks*, 2(5):359–366, 1989. ISSN 0893-6080. doi: https://doi.org/10.1016/0893-6080(89)90020-8. URL `https://www.sciencedirect.com/science/article/pii/0893608089900208`.

Y. Iida, Y. Takatani, A. Kojima, and M. Ishii. Global trends of ocean co2 sink and ocean acidification: an observation-based reconstruction of surface ocean inorganic carbon variables. *Journal of Oceanography*, 77(2):323–358, Apr 2021. ISSN 1573-868X. doi: 10.1007/s10872-020-00571-5. URL https://doi.org/10.1007/s10872-020-00571-5.

K. S. Johnson, J. N. Plant, L. J. Coletti, H. W. Jannasch, C. M. Sakamoto, S. C. Riser, D. D. Swift, N. L. Williams, E. Boss, N. Haëntjens, L. D. Talley, and J. L. Sarmiento. Biogeochemical sensor performance in the soccom profiling float array. *Journal of Geophysical Research: Oceans*, 122(8): 6416–6436, 2017. doi: https://doi.org/10.1002/2017JC012838. URL https://agupubs.onlinelibrary.wiley.com/doi/abs/10.1002/2017JC012838.

P. Landschützer, N. Gruber, and D. C. E. Bakker. Decadal variations and trends of the global ocean carbon sink. *Global Biogeochemical Cycles*, 30(10): 1396–1417, 2016. doi: https://doi.org/10.1002/2015GB005359. URL https://agupubs.onlinelibrary.wiley.com/doi/abs/10.1002/2015GB005359.

A. Olsen, R. M. Key, S. van Heuven, S. K. Lauvset, A. Velo, X. Lin, C. Schirnick, A. Kozyr, T. Tanhua, M. Hoppema, S. Jutterström, R. Steinfeldt, E. Jeansson, M. Ishii, F. F. Pérez, and T. Suzuki. The global ocean data analysis project version 2 (glodapv2) – an internally consistent data product for the world ocean, 2016. URL https://essd.copernicus.org/articles/8/297/2016/.

J. C. Orr and J.-M. Epitalon. Improved routines to model the ocean carbonate system: mocsy 2.0. *Geoscientific Model Development*, 8(3):485–499, 2015. doi: 10.5194/gmd-8-485-2015. URL https://gmd.copernicus.org/articles/8/485/2015/.

M. Reichstein, G. Camps-Valls, B. Stevens, M. Jung, J. Denzler, N. Carvalhais, and Prabhat. Deep learning and process understanding for data-driven earth system science. *Nature*, 566(7743):195–204, Feb 2019. ISSN 1476-4687. doi: 10.1038/s41586-019-0912-1. URL https://doi.org/10.1038/s41586-019-0912-1.

C. Rödenbeck, T. DeVries, J. Hauck, C. Le Quéré, and R. F. Keeling. Data-based estimates of interannual sea–air $co_2$ flux variations 1957–2020 and their relation to environmental drivers. *Biogeosciences*, 19(10):2627–2652, 2022. doi: 10.5194/bg-19-2627-2022. URL https://bg.copernicus.org/articles/19/2627/2022/.

J. Zeng, Y. Iida, T. Matsunaga, and T. Shirai. Surface ocean co2 concentration and air-sea flux estimate by machine learning with modelled variable trends. *Frontiers in Marine Science*, 9, 2022. ISSN 2296-7745. doi: 10.3389/fmars.2022.989233. URL https://www.frontiersin.org/articles/10.3389/fmars.2022.989233.